Main Manuscript for

Fluoro-Organosulfur Catholytes to Boost Lithium Primary Battery Energy

Haining Gao[1], Alejandro Sevilla[2], Gustavo M. Hobold[2], Aaron Melemed[2], Rui Guo[2], Simon C. Jones[3], Betar M. Gallant[2]*

[1]Department of Materials Science and Engineering, Massachusetts Institute of Technology; 77 Massachusetts Avenue, Cambridge, Massachusetts 02139, United States.

[2]Department of Mechanical Engineering, Massachusetts Institute of Technology; 77 Massachusetts Avenue, Cambridge, Massachusetts 02139, United States.

[3]Division of Chemistry and Chemical Engineering, California Institute of Technology; Pasadena, California 91125, United States.

*Corresponding author: Betar M. Gallant

Email: bgallant@mit.edu

Author contributions: Conceptualization: H.G. and B.M.G.; Methodology: H.G., B.M.G., and S.C.J.; Investigation: H.G., A.S., G.M.H., A.M., and R.G.; Visualization: H.G. and B.M.G.; Funding acquisition: B.M.G.; Writing – original draft: H.G. and B.M.G.; Writing – review & editing: H.G., B.M.G., S.C.J., and A.S.

Competing Interest Statement: The authors declare that they have no competing interests.

Classification: Physical Sciences-Applied Physical Sciences

Keywords: Li primary battery | high energy density| fluorinated catholyte | sulfur redox

This PDF file includes:

Main Text

Figures 1 to 4

Abstract

Discovery of new electrochemical redox motifs are essential to expand the design landscape for energy-dense batteries. We report a family of fluorinated reactants based on pentafluorosulfanyl arenes that allow for high electron-transfer numbers (up to 8-e^-/reactant) by exploiting multiple coupled redox processes including extensive S–F bond breaking, yielding capacities of 861 $mAh \cdot g_{reactant}^{-1}$ and voltages up to ~2.9 V when used as catholytes in primary Li cells. At a cell level, gravimetric energies of 1085 $Wh \cdot kg^{-1}$ are attained at moderate temperatures of 50 ºC, with 853 $Wh \cdot kg^{-1}$ delivered at >100 $W \cdot kg^{-1}$, exceeding all leading primary batteries based on electrode + electrolyte (sub-stack) mass. Voltage compatibility of *R-Ph-SF_5* reactants and carbon monofluoride (CF_x) conversion cathodes further enabled investigation of a hybrid battery containing both fluorinated catholyte and cathode. The hybrid cells reach extraordinarily high cell active mass loading (~80%) and allow for significant boosting of sub-stack gravimetric energy of Li−CF_x cells by at least 20% while exhibiting good shelf life and safety characteristics.

Significance Statement

To widen the design space for advanced batteries, developing new electrochemical conversion reactions is challenging yet critical. Primary Li batteries have the highest energy densities among all battery technologies, owing to the successful exploitation of light-weight non-transition-metal redox centers, and thus represent exemplar systems for maximizing energy storage in chemical bonds. Here we report a novel class of fluoro-organosulfur catholyte that allows up to 8-e^- transfer per molecule and boosts the energy of the leading Li primary battery chemistry (Li−CF_x) by 20% based on electrode+electrolyte weight. More broadly, we illuminate an unpreceded electrochemical mechanism exploiting full defluorination of S–F bonds, opening new strategies to tailor S-based redox systems of broader relevance to the battery field.

Main Text

Introduction

Extending the classes of reactions that underlie electrochemical energy storage systems is of fundamental and practical importance to enable improved mobility, autonomy, medical devices and electronics. Li-ion batteries rely on reversible electrochemical Li^+ insertion with transition-metal redox centers (Mn, Fe, Co, Ni) comprising metal-oxygen or metal-polyanion bonds (1, 2), which permit l−2 electrons transferred/active-metal site although limit gravimetric energy (~500 $Wh{\cdot}kg_{active\text{-}material}^{-1}$ or ~260 $Wh{\cdot}kg_{packaged}^{-1}$) (3, 4). Primary Li batteries, which fill critical needs in healthcare, autonomy, and many other applications where reliability is requisite, surpass the limits of Li-ion batteries by utilizing lighter electroactive units based on non-transition-metal redox centers such as carbon or sulfur. This substantially lessens the weight per electrical charge (5), although their electrochemistry is not reversible so these batteries are not rechargeable. Such commercial batteries include Li−carbon monofluoride (Li−CF_x), Li−thionyl chloride (Li−$SOCl_2$) and Li−SO_2, with energy densities ranging from 200−800 $Wh{\cdot}kg_{packaged}^{-1}$ and 400−1160 $Wh{\cdot}L_{packaged}^{-1}$ (**Table S1**). Li−CF_x has the highest energy, reaching up to 800 $Wh{\cdot}kg_{packaged}^{-1}$ in low-rate, high-energy cells and offers good safety and storage characteristics due to the solid nature of the CF_x cathode. However, Li−CF_x has limited performance at higher discharge rates (6). Alternatively, Li−$SOCl_2$ and Li−SO_2 offer a broader range of operation for high delivered energy, but these cells incorporate corrosive and easily vaporized sulfur-based catholytes and are limited to specialty applications due to the associated safety concerns. The Li-primary battery field is quite mature, with very few fundamental innovations in cell chemistries in the past 40 years (7, 8).

The redox centers of carbon (+4 to −4), nitrogen (+3 to −5), sulfur (+6 to −2), or phosphorus (+3 to −5) are of particular interest to exploit for advanced battery formulations given their light

weight and large theoretically-accessible electron transfer numbers. Sulfur (S)-based redox has received particular focus given the reversibility of its lowest oxidation states (0 to −2) as exploited in rechargeable Li−S batteries (9, 10). The higher range of sulfur's oxidation states have been realized in commercial primary chemistries based on (halo)oxides, *viz.* Li−$SOCl_2$ (S oxidation state: +4 to 0) (11), Li−SO_2 (+4 to +3) (12, 13), and in Li−SO_2Cl_2 (+6 to +4) (14). Motivated by earlier development of stored chemical energy propulsion systems that employ a thermochemical reaction between molten Li and sulfur hexafluoride (SF_6) gas at 500−600 ˚C (15), we previously developed a room-temperature electrochemical analogue in the form of a primary Li battery with SF_6 dissolved in an organic electrolyte (16). The cell discharge reaction is $SF_6 + 8Li \rightarrow 6LiF + Li_2S$, analogous to the thermochemical system, and thus successfully exploits the full oxidation-state range of sulfur (+6 to −2). In spite of unrivaled high theoretical energy densities of 3920 $Wh{\cdot}kg_{Li+SF6}^{-1}$ based on weight of reactants, Li−SF_6 cells exhibited sluggish discharge reactions in practice associated with low gas solubilities (~1−5 mM) and hindered activation of symmetric SF_6 in which octahedrally-coordinated F^- ligands shield the redox-active S^{6+} center (17), making this first generation of S−F redox systems of scientific interest but unable to fully realize the intrinsically high energy density.

Here we demonstrate that these challenges can be overcome through design of catholytes that extensively exploit S−F bond electroactivity (**Fig. 1A**), providing high delivered energy with facile kinetics. We examined the family of pentafluorosulfanyl arenes (18, 19) with the formula *R-Ph-SF_5*, where *Ph* is a phenyl ring and *R* is an electron-withdrawing group. When used as a catholyte in Li−carbon cells, *R-Ph-SF_5* reactants are found to undergo complete defluorination (corresponding to 5-e^-, or 1-e^- per fluoride) with additional reduction possible up to a total of 8-e^- transfer per molecule, yielding competitive gravimetric energies up to 1845 $Wh{\cdot}kg_{Li+R\text{-}Ph\text{-}SF5}^{-1}$ and excellent rate capability. Inspection of the discharge pathways illuminates a coupling of S−F

bond cleavage with further S-based redox that is highly sensitive to the reactant structure and *R*-group functionality, providing multiple motifs for design and manipulation of electrochemical defluorination reactions as an emerging class of high-capacity and energy-dense storage vectors. Practically, voltage compatibility of *R-Ph-SF₅* and solid CF_x cathodes further enables design of a hybrid battery that achieves remarkably high active mass loading in the cell, boosting the attainable gravimetric energy of Li−CF_x batteries by a minimum of 20%.

Results and discussion

Intrinsic electroactivity and products of R-Ph-SF₅ discharge

The reactant structures and their incorporation into a Li primary battery are shown in **Fig. 1**. *R-Ph-SF₅* reactants exhibit multiple design handles, including the nature of the aromatic group, R-group composition and position (**Fig. 1B**). Compared to SF_6(g), molecular structure and lowest unoccupied molecular orbital (LUMO) calculations (**Fig. S1**) show that the aromatic group of *R-Ph-SF₅* breaks the S−F symmetry while retaining a similar electronic structure around the sulfur redox center. The aromatic group also imparts miscibility with organic solvents up to 5 M concentration (**Fig. S2**). Notably, *R-Ph-SF₅*-class reactants have safety ratings favorable to both $SOCl_2$ and typical Li-ion electrolyte formulations due to low corrosivity, low flammability, high boiling point and high chemical stability (**Table S2**). Cells (**Fig. 1A**) were assembled with a Li metal anode, a carbon cathode substrate (Ketjen black or carbon foam), and a catholyte comprising *R-Ph-SF₅* (0.1−5 M) with $LiClO_4$ salt and dimethyl sulfoxide (DMSO) solvent. $LiClO_4$ was used to avoid additional sources of F for characterization purposes whereas the use of additional DMSO solvent was necessary to dissolve electrolyte salt. In addition, DMSO was shown previously to support high capacities of fluoride conversion cathodes given the ability to partially solubilize LiF (17).

To examine the intrinsic redox behavior, **Fig. 1C** shows discharge of cells containing 0.1 M *R-Ph-SF₅* at 40 μA/cm^2 as a function of electrons reacted per molecule (calculation details in supplementary note 2). Cells were tested at 50 ºC to maximize capacity; temperature effects are revisited later. Unsubstituted *Ph-SF₅* and *Ph-I-SF₅* exhibited modest voltages of ~2.5 V vs. Li/Li$^+$ over a single plateau. Increasing the Hammett coefficient of the electron-withdrawing functionality to −NO_2 in the meta (*m*) or para (*p*) position (0.71 or 0.78, *vs.* 0.18 for –I at para) **(20)** led to higher discharge voltages. The highest cell voltage was obtained with −NO_2 in the para (*p*) position and yielded a three-stage discharge profile with plateaus at 2.9, 2.3 and 2.1 V vs. Li/Li$^+$ with a total capacity of 8 e$^-$/molecule (861 mAh·$g_{R\text{-}Ph\text{-}SF5}^{-1}$, identical to the theoretical capacity; **Fig. S3**). Given its leading performance, all subsequent studies utilize *p-NO₂-Ph-SF₅* with the *'p'* henceforth omitted.

To examine the conversion process in detail, 0.1 M NO_2-Ph-SF_5 was discharged to varying terminal voltages (**Fig. 2A**) after which cathodes and/or electrolyte were extracted for analysis. At 2.54−2.38 V vs. Li/Li$^+$, the cathodes consisted of cubic crystallites of ~270 ± 50 nm in **Fig. 2B** (SEM of a pristine cathode in **Fig. S4**), confirmed to be LiF (rocksalt, $Fm\bar{3}m$) from X-ray diffraction (**Fig. S5**) and in the XPS F 1s spectrum (684.9 eV, **Fig. 2C**). Given the electronically insulating nature of LiF, the energy-minimized structure and large particle size suggests that LiF particles grow *via* a solution-mediated process (17, 21). The amount of solid sulfur products in the cathode S 2p spectra was negligible (< 0.1 at. %, **Fig. 2D** and **Fig. S6A**) (22) after the high-voltage plateau, however, ultraviolet-visible (UV-vis) spectroscopy and visual analysis confirmed that most of the sulfur was present in solution as polysulfides, with S_8^{2-} predominant (**Fig. 2E**, **2F**). The data collectively indicate that the high-voltage plateau corresponds to near-stoichiometric defluorination of all 5 F ligands in Ph-NO_2-SF_5, a process that liberates S intermediates from the

parent molecule which then undergo polymerization reactions in solution. Polysulfide generation continued upon further discharge to 2.07 V vs. Li/Li^+ (~ 1 e^-), with a slight increase in cathode S content (to ~0.8 at. %, **Fig. 2D**).

Full discharge to 1.90 V vs. Li/Li^+ c led to near-complete disappearance of any species detected by UV-vis (23) (**Fig. 2E**) and XPS indicated a modest increase in the cathode's S and N content (to ~1.5 and 1.3 at.%, respectively, **Fig. 2D** and **Fig. S6A-C**). Prior studies have reported the tendency of nitro-functionalized aromatics to react with short-chain (S_2^{2-}) polysulfides in DMSO and undergo ring thiol substitution with NO_2^- as a leaving group (24), a possible mechanism that could account for S-poor solid phases in discharged cathodes and retention of reduced S in the liquid phase, along with minor increases in N. O content in the cathode also increased from 16.8 to 27.0 at.% between 2.07 and 1.90 V vs. Li/Li^+ (**Fig. 2D** and **Fig. S6C**), while corresponding SEM images indicated nucleation of a new phase with spherical morphology (**Fig. 2B**), confirmed to be O-rich and N, F, S-poor by energy-dispersive X-ray analysis (**Fig. S7**). The XPS O 1s (**Fig. S6D**) and Raman spectrum (**Fig. S6E**) indicated this phase to be Li_2CO_3, which might arise from $-NO_2$-derived interactions with DMSO or prior formation of Li_2O, a plausible reduction product of the nitro group that could react further with electrolyte or trace CO_2 to yield Li_2CO_3. These spherical particles formed only with $-NO_2$ containing reactants and regardless of salt, excluding the possibility that they originate from $LiClO_4$ (**Fig. S8**). Significantly, cell headspace analysis by gas chromatography and mass spectroscopy (**Fig. S9**) ruled out formation of NO, NO_2, or N_2O, and cells discharged with a pressure transducer showed negligible gas evolution (**Fig. S10**) of any kind. While the precise mechanism of multi-electron NO_2-Ph-SF_5 reduction is complex, the overall mechanism indicates extensive S−F, S−S, C−S, and N−O bond activation and reduction, yielding solid and liquid products that accumulate throughout the cell.

Discharge performance of Li−NO_2-Ph-SF_5 cells

The electrochemical performance was examined as a function of reactant concentration to evaluate feasibility as a high-concentration catholyte. **Fig. 3A** shows galvanostatic discharge at concentrations of 1−5 M at 40 μA/cm^2, where capacities are here normalized to the weight of NO_2-Ph-SF_5 as an intrinsic measure of reactant utilization. Discharge at concentrations of 1.0−2.0 M led to attainable capacities of 818 and 786 mAh·$g_{NO2\text{-}Ph\text{-}SF5}^{-1}$ respectively, with retention of a similar discharge profile. Further increasing concentration (≥3 M) saw disappearance of the lower-voltage plateau at ~2.1 V vs. Li/Li^+, with capacities of 544 mAh·$g_{NO2\text{-}Ph\text{-}SF5}^{-1}$ attained at 5.0 M. The loss of the lower-voltage plateau indicates that the carbon cathode surface became passivated by LiF at high potentials before NO_2-Ph-SF_5 could be fully reduced, *i.e.*, cells switched from being reactant-limited to surface passivation-limited. This was confirmed by SEM of discharged cathodes showing extensive crystallization of cubic LiF particles and no visible carbon substrate remaining (**Fig. 3B** *vs.* **Fig. 2B**).

In spite of lower per-molecule utilization, increasing the concentration enables improved cell-level metrics. **Fig. S11** plots the same data in **Fig. 3A** at 40 μA/cm^2 in units of total or areal capacity, showing a monotonic increase from 5.8−19.1 mAh·cm^{-2} between 1.0 and 5.0 M. To accurately represent the cell performance on a gravimetric basis, normalization was additionally conducted based on the weight of all cell materials (*i.e.* NO_2-Ph-SF_5 + electrolyte + carbon cathode + consumed Li) excluding only the current collectors, separator, binder, and cell housing (25), henceforth denoted as "sub-stack". **Fig. 3C** shows these sub-stack capacities and gravimetric energies at a slightly higher current of 0.1 mA·cm^{-2} (**Fig. S12**). Capacities increased from 292 to 362 mAh·$g_{sub\text{-}stack}^{-1}$ as concentration increased from 3 M to 4 M, beyond which further gains were negligible. The maximum gravimetric energy of 1085 Wh·$kg_{sub\text{-}stack}^{-1}$ was obtained at 4.5 M. Capacity and energy decreased with concentrations exceeding 4.5 M due to diminishing supporting

solvent (DMSO, ~16 wt% of the catholyte at 5 M) which led to significant decline in ionic conductivity from 6.4 to 0.6 $mS \cdot cm^{-1}$ from 0.1 M to 5 M (**Fig. S13**). Additionally, low DMSO content decreases the ability to solubilize LiF, making electrode passivation effects more severe. The rate capability of cells at 4.0 M concentration is shown in **Fig. 3D** and the corresponding rate-dependent LiF morphology is shown in **Fig. S14**. Capacities remained constant at ~362 $mAh \cdot g_{sub\text{-}stack}^{-1}$ from 0.3 – 1.0 $mA \cdot cm^{-2}$ (0.01 C − 0.04 C-rate; calculation in supplementary note 5) and decreased moderately thereafter up to 3 $mA \cdot cm^{-2}$ (0.12 C), indicating excellent rate capability. Critically for primary battery applications, **Fig. S15** shows that as-assembled Li−NO_2-Ph-SF_5 cells rested for 30 days at 50 ˚C exhibited no capacity loss upon subsequent discharge, and cells also exhibited negligible voltage fade upon interruption at partial depth-of-discharge and resting for 10−30 days, indicating good shelf life characteristics.

To compare performance with state-of-the-art primary batteries, Li−CF_x cells were assembled and tested (**Fig. S16**). The breakdown of the cell masses is shown in **Fig. 4A**. Typical electrolyte-to-active solid mass fractions in commercial cells range from 0.7–1.3 (26, 27), a lean electrolyte loading that is challenging to achieve in-house. Consequently, Li−CF_x cells (20.4 ± 2.3 mg of CF_x, 11.5 ± 1.3 $mg \cdot cm^{-2}$ loading) were tested in a flooded electrolyte configuration but normalized assuming a 1:1 electrolyte:cathode mass ratio dictated by commercial standards. In Li−NO_2-Ph-SF_5 cells, the active material is in the liquid phase, hence design considerations favor a substantially larger electrolyte-to-solid ratio (carbon being electrochemically inactive) of ~8:1 w/w, with 5 $mg \cdot cm^{-2}$ of carbon and ~28 $mg \cdot cm^{-2}$ of NO_2-Ph-SF_5 for 4 M concentration. A Ragone plot in **Fig. 4B** shows that Li−NO_2-Ph-SF_5 cells attain comparable sub-stack level performance to Li−CF_x cells at low power (~1000 $Wh \cdot kg_{sub\text{-}stack}^{-1}$ at ~15 $W \cdot kg_{sub\text{-}stack}^{-1}$). These values compare to active-mass theoretical values of 1845 $Wh \cdot kg_{active}^{-1}$ (Li−NO_2-Ph-SF_5) and 2050 $Wh \cdot kg_{active}^{-1}$ (Li−CF_x), which, in contrast to sub-stack metrics, omit inactive electrolyte/carbon (**Table S1**). The

numbers indicate the following: First, both cell formulations, as expected, exhibit significant decreases in gravimetric energy when inactive masses (electrolyte + carbon) are accounted for on the more-realistic sub-stack basis. Second, Li−NO_2-Ph-SF_5 cells with liquid reactants exhibit proportionally higher active mass utilization, which in turn enables comparable or higher cell energies in practice. This gain arises from the ability to minimize dead weight of electrolyte compared to Li−CF_x (both cells utilize comparable inactive C). Moreover, Li−NO_2-Ph-SF_5 cells show advantages over Li−CF_x at moderate powers (50−100 $W \cdot kg_{sub\text{-}stack}^{-1}$) which is attributed to facile kinetics in the liquid phase. These gains diminish at higher powers (>150 $W \cdot kg_{sub\text{-}stack}^{-1}$) for this particular formulation due to limitations of ionic conductivity of NO_2-Ph-SF_5-based electrolytes, which will require future studies to engineer and optimize.

Hybrid solid-liquid cell design

The chemical compatibility and voltage matching of Li−NO_2-Ph-SF_5 and Li−CF_x creates new possibilities to design hybrid cell concepts that surpass the gravimetric energy of any known formulation (**Fig. S17**) (28, 29). To demonstrate this, we designed cells containing a NO_2-Ph-SF_5:CF_x mass ratio of ~2:1 (**Fig. 4A** and **Fig. S18**). The total sub-stack percentage of active materials was ~80%, compared to the Li−CF_x (~50%) or Li−NO_2-Ph-SF_5 cells (~70%). A gravimetric capacity of 421 $mAh \cdot g_{sub\text{-}stack}^{-1}$ was obtained at 0.1 $mA \cdot cm^{-2}$ with the hybrid cell, significantly higher than the respective individual cells (≤362 $mAh \cdot g_{sub\text{-}stack}^{-1}$, **Fig. 4C**). The gravimetric energy, reaching 1195 $Wh \cdot kg_{sub\text{-}stack}^{-1}$ at 5 $W \cdot kg_{sub\text{-}stack}^{-1}$, represents a ~20% improvement over Li−CF_x at the sub-stack level (**Fig. 4B**). SEM images (**Fig. 4D**) of discharged cells showed formation of LiF crystallites on CF_x graphite flakes that were not present in CF_x-only cells, further confirming utilization of both solid and liquid capacities. We note that the hybrid cell utilized a commercial CF_x powder blend optimized for conventional cell performance and does not necessarily provide optimal surface area to accommodate NO_2-Ph-SF_5 discharge, which may

be improved through future development. Indeed, higher rates in the hybrid cell configuration led to decreasing capacity due to premature passivation by LiF (**Fig. S19A**). Thus, as a second example of hybrid cell design for higher power, reactant concentrations were lowered to 3.5 M and temperatures were increased to 70 ˚C. At 2.0 $mA \cdot cm^{-2}$, a capacity of 363 $mAh \cdot g_{sub\text{-}stack}^{-1}$ was obtained, corresponding to a 38% capacity increase than that obtained at 50 ˚C with 4 M NO_2-Ph-SF_5 (**Fig. S19**).

We emphasize that these metrics, which demonstrate several pathways to exceed performance of commercial CF_x at mild temperature (50−70 ˚C), were tested in cells subjected to limited optimization. Further improvements in cell performance are envisioned possible with continued development, including cell conditions that can finely-tune electrolyte-to-solid ratios. The theoretical expected energy of a hybrid cell is computed in **Fig. S20** and indicates that maximum performance for 5 M reactant occurs around a NO_2-Ph-SF_5:CF_x mass ratio of 1:1.1 and 627 $mAh \cdot g_{sub\text{-}stack}^{-1}$, a ~50% increase compared to the above numbers attained in practice so far.

Temperature effects

Additional efforts are needed to realize competitive operation of fluorinated liquid cathode batteries at room temperatures. Without heating, the high-voltage discharge plateau exhibits truncation and capacities that are 15−20% lower (**Fig. S21**). Rate effects are also more severe (**Fig. S22**), which may result from hindered transport, *e.g.* decreased diffusivity of reactant or LiF product solubility, noting that ionic conductivities were not strongly sensitive to temperature (**Fig. S13**). Future improvements lie with all aspects of electrolyte engineering, including reactant, solvent, and salt to balance the demands for high reactant solubility, high salt solubility, and low viscosities throughout discharge. Second, cathode engineering to tailor active surface and pore sizes may help to accommodate larger amounts of LiF prior to passivation, allowing improved

performance at lower temperatures. Temperature effects on the Li anode should also not be overlooked: at 50 °C, Li anodes from Li−NO_2-Ph-SF_5 cells rested for one week showed, *via* SEM and electrochemical impedance spectroscopy, growth and stabilization of a ~200 nm thick solid electrolyte interphase (SEI) consisting primarily of LiF (**Fig. S23**). This SEI can effectively protect the Li anode against sustained parasitic reactivity. At room temperature, LiF particles on Li were sparser and smaller, even after resting for one week (**Fig. S24**). The results suggest that Li anode engineering to favor optimal SEI growth is a compelling future direction.

Conclusions

Through molecular design, advanced catholytes have been developed that successfully exploit the wide oxidation state window of S in non-metal-containing, lightweight reactants. These catholytes yield high capacities and permit high cell active mass loadings, enabling the gravimetric energy of all known Li primary batteries to be exceeded at a sub-stack level. Handles to further tailor capacity, voltage, and kinetics in fluorosulfur catholytes at a fundamental level include number and positioning of fluoride/halide ligands, chemical and electronic structure of the aromatic group, its linker to the $-SF_5$ moiety, and R-group functionality. At the cell level, the wide landscape for electrolyte design and solid-liquid balancing highlight significant remaining room for improvement. Although lowering the temperature requirements is attractive, many battery technologies operate at mildly elevated temperatures either intrinsically (due to operation requirements) (5) or reach such temperatures due to self-heating (30); there is no intrinsic limitation identified at present to prevent competitive metrics at room temperature if key challenges can be addressed. Looking ahead, learning how to adapt S-based molecular redox to achieve both large oxidation state changes and reversibility is tantalizing and remains a grand challenge for future high-energy battery development.

Materials and Methods

Chemicals and Materials. 4-nitrophenylsulfur pentafluoride (*p*-NO_2-Ph-SF_5, >96%, TCI), 4-iodophenylsulfur pentafluoride (*p*-I-Ph-SF_5(*p*), >94%, TCI), phenylsulfur pentafluoride (Ph-SF_5, >98%, TCI), 3-nitrophenylsulfur pentafluoride (*m*-NO_2-Ph-SF_5, Synquest), dimethylsulfoxide (DMSO, anhydrous, > 99.9%, Sigma-Aldrich), and 1,2-dimethoxyethane (DME, 99.5%, Sigma-Aldrich) were stored inside an argon-filled glovebox (H_2O content <0.5 ppm, O_2 content <0.3 ppm, MBRAUN). The density of *p*-NO_2-Ph-SF_5 in the liquid state is 1.60 ± 0.04 g·mL^{-1}, which was determined by measuring the weight of 1 mL *p*-NO_2-Ph-SF_5 liquid upon heating to just above the melting temperature (30−40 ˚C). $LiClO_4$ (99.99% trace metals basis, Sigma-Aldrich) and Whatman filter paper (Grade QM-A, 2.2 μm pore size, 450 μm thickness, Sigma-Aldrich) were dried in a Buchi glass oven under active vacuum for 24 hours at 120 °C prior to transferring into the glovebox.

Cathode Preparation. All electrodes were dried under active vacuum in a glass oven (Buchi) overnight at 90 °C and stored in an Ar glovebox. Ketjen black (KB) electrodes used in Fig. 1 and 2 were fabricated in-house by uniformly coating sonicated inks composed of KB powder (AzkoNobel), N-methyl-2-pyrrolidone (NMP), and polyvinylidene difluoride (PVDF) binder (weight ratio of KB:PVDF = 80:20) onto a sheet of Toray paper (TGP-H-030, 5% wet proofing, Fuel Cell Earth). The resulting carbon loading was 0.6 ± 0.1 mg·cm^{-2} (average and error bar based on ten measurements). The obtained coated Toray paper was dried at room temperature and then punched into circular disks (12 mm diameter) prior to further drying as indicated above. Carbon foam cathodes (gas diffusion layer coated with a microporous layer, EQ-bcgdl-1400S-LD, MTI Corp.) used in Fig. 3 and 4 has a carbon loading reported as 5 mg·cm^{-2}. The as-received carbon foam was punched into 15 mm-diameter disks and dried as above. The CF_x powder mix has a CF_x (ARC 1000)/carbon/polytetrafluoroethylene (PTFE) ratio of 85/10/5. The as-received powder mix was rolled into a film and punched into circular disks with a diameter of 15 mm before drying. The typical CF_x loading of the obtained electrode is 11.5 ± 1.3 mg·cm^{-2} (based on ten measurements).

Galvanostatic Discharge. All the cells were constructed in the argon glovebox and consisted of carbon or CF_x as the cathode substrate, a Li metal disk as anode (0.75 mm thick, 99.9% metals

basis, Alfa Aesar). The separator (Whatman filter paper) was impregnated with 50 μL of catholyte solution (cell assembling details in Supplementary Information). All cells were rested at open circuit voltage (OCV) for 5 h before initiating galvanostatic discharge. All discharge tests (BioLogic VMP3 potentiostat or MPG2 workstation) were conducted at the indicated current density with a voltage window ranging from OCV (typically ~2.9 (Li−CF_x), ~3.0 (Li−*m*-NO_2-Ph-SF_5), ~3.2 (Li−*p*-NO_2-Ph-SF_5), ~3.3 (Li−*p*-I-Ph-SF_5), ~3.4 (Li−Ph-SF_5) V vs. Li/Li^+) to a lower voltage cutoff of 1.9 V vs Li/Li^+. For galvanostatic discharge at 50 or 70 °C, cells were placed inside an incubator (Memmert GmbH + Co. KG).

Scanning Electron Microscopy (SEM). Following discharge, cells were disassembled inside the glovebox and the cathode substrate and/or Li anode were extracted, rinsed with DME, and dried in the argon glovebox. For cathode characterization, samples were sealed in a glass vial in the glovebox and quickly transferred into the SEM chamber to minimize exposure to ambient. For characterization of Li anodes, samples were sealed in an air-sensitive holder in the glovebox and transferred to the SEM chamber without exposure to ambient. All SEM characterization was conducted on a Zeiss Merlin high-resolution SEM operating at an accelerating voltage of 5 kV and beam current of 100 pA.

Spectroscopy. Discharged cathode substrates were harvested from cells inside the glovebox and dried under vacuum overnight at room temperature. XPS analysis was conducted on a PHI VersaProbe II X-ray Photoelectron Spectrometer. The binding energies were calibrated by the LiF peak at 684.90 eV, except for the pristine carbon sample without LiF, in which case energies were calibrated to the C−F binder peak at 688.40 eV. High-resolution spectra were deconvoluted using CasaXPS software with a Shirley-type background and a 70% Gaussian/30% Lorentzian line shape. Ultraviolet-visible (UV-vis) spectroscopy measurements were conducted using an Agilent Cary 60 UV-vis spectrometer. To prepare samples, the separator was harvested from the discharged cell inside the glovebox and soaked in 1 mL DMSO. The resulting solution was then diluted by ~20x for UV-vis measurements inside the glovebox, and 1 mL of this diluted solution

was transferred to a cuvette and sealed under Ar. A typical UV-vis measurement (including scan time) takes around 10 minutes.

Acknowledgments

The authors gratefully acknowledge funding from the MIT Lincoln Laboratory and from the Army Research Office under award number W911NF-19-1-0311. This work made use of the MRSEC Shared Experimental Facilities at MIT, supported by the National Science Foundation under award number DMR-14-19807. We gratefully acknowledge Dr. Kevin Tibbetts at MIT Lincoln Laboratory for insightful discussions.

References

1. Whittingham M. S., Ultimate limits to intercalation reactions for lithium batteries. *Chem. Rev.* **114**, 11414-11443 (2014).
2. Liu J.*, et al.*, Pathways for practical high-energy long-cycling lithium metal batteries. *Nat. Energy* **4**, 180-186 (2019).
3. Schmuch R., Wagner R., Hörpel G., Placke T., Winter M., Performance and cost of materials for lithium-based rechargeable automotive batteries. *Nat. Energy* **3**, 267-278 (2018).
4. Nitta N., Wu F., Lee J. T., Yushin G., Li-ion battery materials: present and future. *Mater. Today* **18**, 252-264 (2015).
5. Reddy T. B. , Linden D., "Lithium primary batteries" in Linden's handbook of batteries (4th Edition)*,* (McGraw-Hill, 2010), pp. 14.1-14.87.
6. Bock D. C., Marschilok A. C., Takeuchi K. J., Takeuchi E. S., Batteries used to power implantable biomedical devices. *Electrochim. Acta* **84**, 155-164 (2012).
7. Dell R., Batteries: fifty years of materials development. *Solid State Ionics* **134**, 139-158 (2000).
8. Reddy M. V., Mauger A., Julien C. M., Paolella A., Zaghib K., Brief history of early lithium-battery development. *Materials* **13**, 1884 (2020).
9. Bruce P. G., Freunberger S. A., Hardwick L. J., Tarascon J.-M., $Li–O_2$ and Li–S batteries with high energy storage. *Nat. Mater.* **11**, 19-29 (2012).

10. Pang Q., Liang X., Kwok C. Y., Nazar L., Advances in lithium–sulfur batteries based on multifunctional cathodes and electrolytes. *Nat. Energy* **1**, 1-11 (2016).
11. Hills A. , Hampson N., The Li-$SOCl_2$ cell—a review. *J. Power Sources* **24**, 253-271 (1988).
12. Fey G.-K., Li/SO_2 rechargeable batteries. *J. Power Sources* **35**, 153-162 (1991).
13. Abraham K. , Chaudhri S., The lithium surface film in the Li/SO_2 cell. *J. Electrochem. Soc.* **133**, 1307 (1986).
14. Abraham K., Chemical and electrochemical processes in some lithium-liquid cathode batteries. *J. Power Sources* **34**, 81-101 (1991).
15. Hughes T., Smith R., Kiely D., Stored chemical energy propulsion system for underwater applications. *J. Energy* **7**, 128-133 (1983).
16. Li Y., Khurram A., Gallant B. M., A high-capacity lithium–gas battery based on sulfur fluoride conversion. *J. Phys. Chem. C* **122**, 7128-7138 (2018).
17. Gao H. , Gallant B. M., Advances in the chemistry and applications of alkali-metal–gas batteries. *Nat. Rev. Chem.* **4**, 566–583 (2020).
18. Sheppard W. A., Arylsulfur pentafluorides. *J. Am. Chem. Soc.* **84**, 3064-3072 (1962).
19. Savoie P. R. , Welch J. T., Preparation and utility of organic pentafluorosulfanyl-containing compounds. *Chem. Rev.* **115**, 1130-1190 (2015).
20. Hansch C., Leo A., Taft R., A survey of Hammett substituent constants and resonance and field parameters. *Chem. Rev.* **91**, 165-195 (1991).
21. Johnson L.*, et al.*, The role of LiO_2 solubility in O_2 reduction in aprotic solvents and its consequences for Li–O_2 batteries. *Nat. Chem.* **6**, 1091 (2014).
22. Liang X.*, et al.*, A highly efficient polysulfide mediator for lithium–sulfur batteries. *Nat. Commun.* **6**, 1-8 (2015).
23. Wild M.*, et al.*, Lithium sulfur batteries, a mechanistic review. *Energy Environ. Sci.* **8**, 3477-3494 (2015).
24. Kornblum N. , Widmer J., Substitution reactions which proceed via radical anion intermediates. 19. Direct conversion of nitro compounds to thiols. *J. Am. Chem. Soc.* **100**, 7086-7088 (1978).
25. Betz J.*, et al.*, Theoretical versus practical energy: a plea for more transparency in the energy calculation of different rechargeable battery systems. *Adv. Energy Mater.* **9**, 1803170 (2019).

26. Muffoletto B. C. , Kuwik R. J., Internal electrode and assembly method for electrochemical cells, U.S. Patent No. 5,250,373 (1993).

27. Probst J., Takeuchi E. S., Smesko S. A., Enhanced capacity Li/CF_x electrochemical cell, U.S. Patent No. 6,451,483 (2002).

28. Zhang X. , Wang X., High Capacity and High Rate Lithium Cells with CF_x-MnO_2 Hybrid Cathode, U.S. Patent Application No. 12/145,665 (2009).

29. Marple J., Performance characteristics of Li/MnO_2-CF_x hybrid cathode jellyroll cells. *J. Power Sources* **19**, 325-335 (1987).

30. Hansen L. D. , Frank H., Kinetics and thermodynamics of chemical reactions in Li/$SOCl_2$ cells. *J. Electrochem. Soc.* **134**, 1 (1987).

31. Zou Q. , Lu Y.-C., Solvent-dictated lithium sulfur redox reactions: an operando UV-vis spectroscopic study. *J. Phys. Chem. Lett.* **7**, 1518-1525 (2016).

32. Bonnaterre R. , Cauquis G., Spectrophotometric study of the electrochemical reduction of sulphur in organic media. *J. Chem. Soc., Chem. Commun.* 293-294 (1972).

Figures

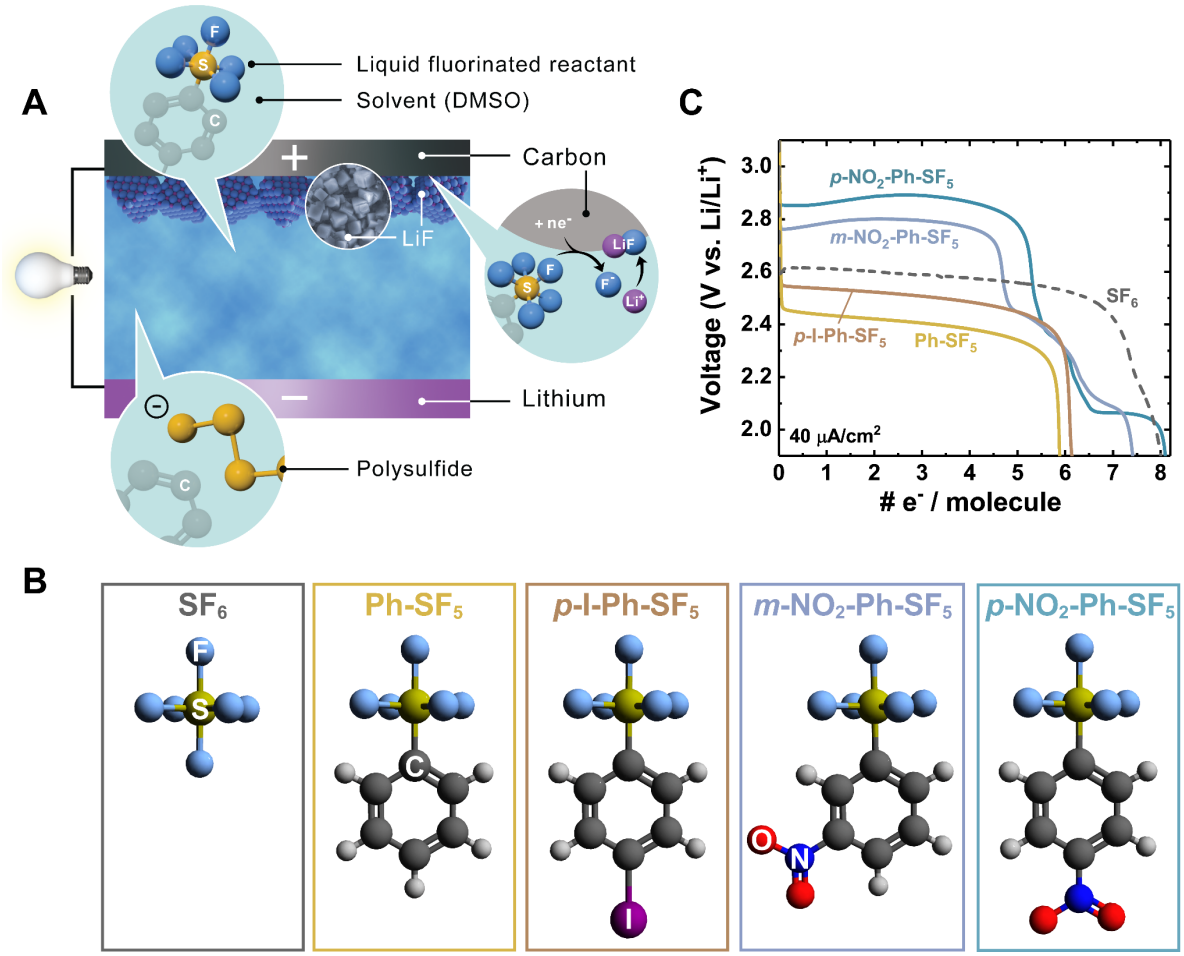

Figure 1. Pentafluorosulfanyl arenes (*R-Ph-SF₅*) as a class of fluorinated catholytes. ***(A)*** Schematic depicting Li–*R-Ph-SF₅* batteries. ***(B)*** Molecular structures of *R-Ph-SF₅* reactants, with the corresponding discharge profiles shown in ***(C)***. All *R-Ph-SF₅* cells were discharged with 0.1 M *R-Ph-SF₅* / 0.1 M $LiClO_4$ / DMSO as catholyte, Ketjen Black as cathode substrate, at 40 μA·cm^{-2} and 50 °C. Li–SF_6 discharge is included in **C** for comparison. Additional cell details are in the Methods section.

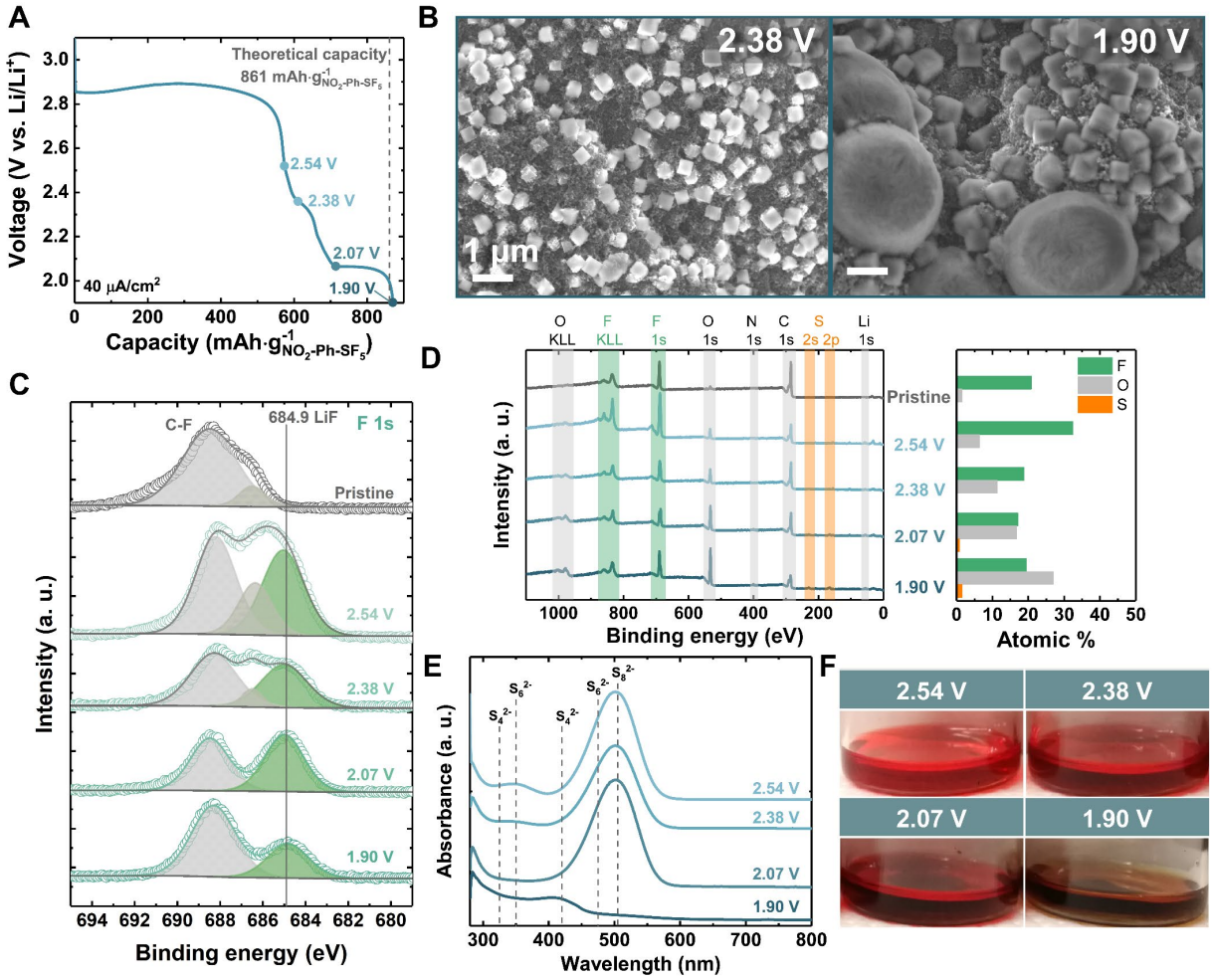

Figure 2. Characterization of NO_2-Ph-SF_5 discharge products. ***(A)*** NO_2-Ph-SF_5 discharge profile under reactant-limited conditions with different cell termination voltages. ***(B)*** SEM of carbon cathodes from cells discharged to 2.38 or 1.90 V vs. Li/Li^+. ***(C)*** High resolution F 1s XPS spectra of discharged electrodes. The two C−F peaks at 688.4 and 686.4 eV are from the polyvinylidene difluoride (PVDF) binder. ***(D)*** XPS survey spectra (left) with corresponding F, O and S atomic percentage (right). ***(E)*** UV-vis spectra of extracted electrolyte from discharged cells (diluted in DMSO) as a function of termination voltage(31, 32). ***(F)*** Corresponding photographs of samples in **E**. All cell conditions as in Fig. 1.

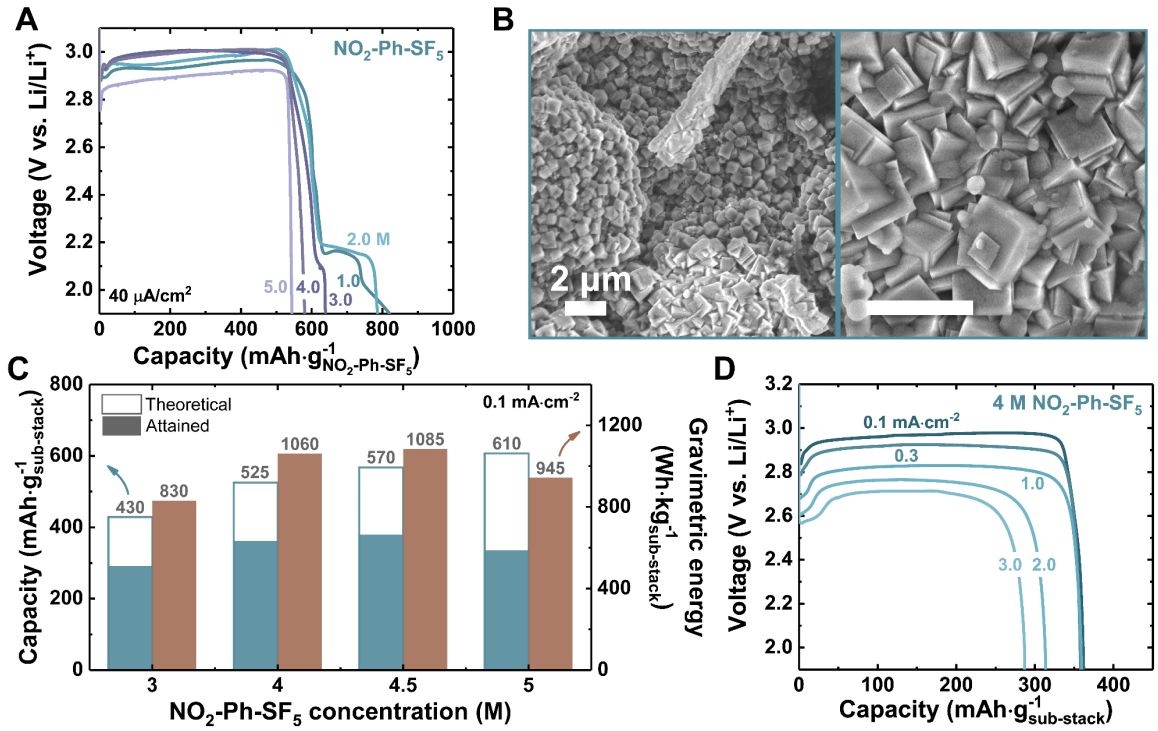

Figure 3. Concentration and rate effects on Li–NO_2-Ph-SF_5 cell discharge. ***(A)*** Galvanostatic discharge of Li–NO_2-Ph-SF_5 cells as a function of NO_2-Ph-SF_5 concentration at 40 μA·cm^{-2}. ***(B)*** SEM of carbon cathodes fully discharged with 3 M NO_2-Ph-SF_5 / 0.2 M $LiClO_4$ / DMSO cathode/electrolyte at 0.3 mA·cm^{-2}. ***(C)*** Theoretical/attained capacities and attained gravimetric energies of Li–NO_2-Ph-SF_5 cells as a function of catholyte concentration. All cells were discharged at 0.1 mA·cm^{-2}. Theoretical capacities correspond to 8 e^- per molecule (calculation details in the supplementary note 3). ***(D)*** Rate capability of cells with 4 M NO_2-Ph-SF_5 / 0.2 M $LiClO_4$ / DMSO. Note that 1 C = ~490 mA·$g_{sub\text{-}stack}^{-1}$ = 24 mA·cm^{-2} at 4 M concentration. 'Sub-stack' weight denotes NO_2-Ph-SF_5 + electrolyte + carbon cathode + consumed Li.

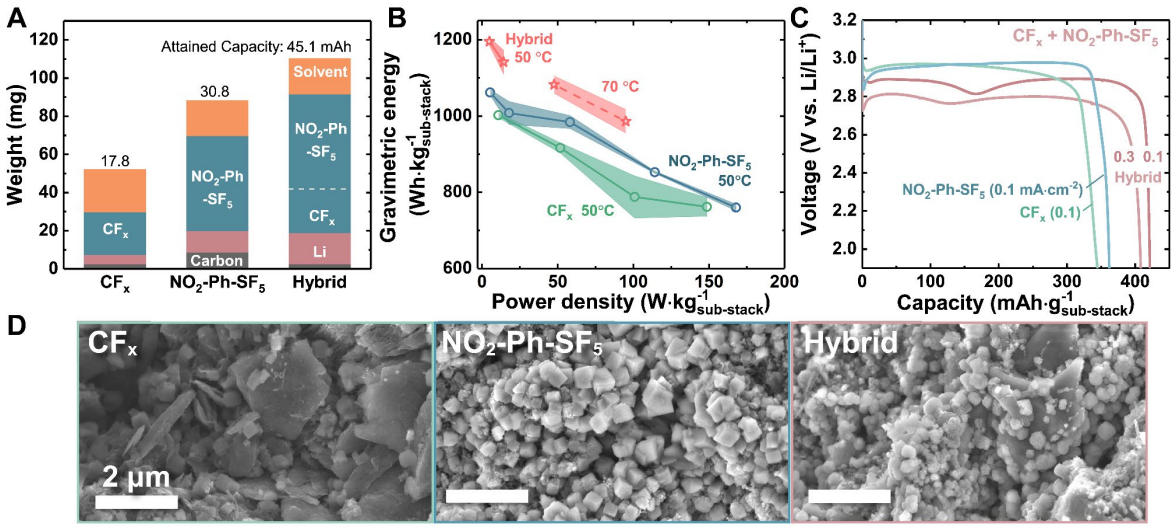

Figure 4. Energy and power of primary Li batteries with fluorinated cathodes and catholytes. ***(A)*** Weight breakdown of cell components in Li−CF_x, Li−NO_2-Ph-SF_5, and hybrid cells. ***(B)*** Ragone plot comparing rate performance of the same cells. Average value and error bar (representing standard deviation) were based on three cells each. ***(C)*** Rate performance of hybrid cells using CF_x as solid cathode and 4 M NO_2-Ph-SF_5 / 0.2 M $LiClO_4$ / DMSO as catholyte. 'Sub-stack' for Li−CF_x denotes CF_x + electrolyte + carbon + consumed Li; for hybrid cells, the weight of NO_2-Ph-SF_5 is also included. ***(D)*** SEM of discharged cathodes from each cell type (0.3 mA·cm^{-2} for Li−NO_2-Ph-SF_5 and hybrid cells, 0.1 mA·cm^{-2} for Li−CF_x).